Para-ferroelectric phase transition driven by swift heavy-ion irradiation in KTN crystal

He, S.; Yang, Q.; Li, X.; Liu, H.; Cao, L.; Akhmadaliev, S.; Wang, X.; Ren, Y.; Zhou, S.; Wu, P.;

Originally published:

April 2020

Applied Surface Science 519(2020), 146261

DOI: https://doi.org/10.1016/j.apsusc.2020.146261

Para-ferroelectric phase transition driven by swift heavy-ion irradiation in KTN crystal

Shan He,[a] Quanxin Yang,[a] Xiaojin Li,[a] Hongliang Liu,[a,c,] Lei Cao[d], Shavkat Akhmadaliev,[d] Xuping Wang,[e] Yingying Ren,[f] Shengqiang Zhou,[d] and Pengfei Wu.[a,b,*]*

[a]Institute of Modern Optics, Nankai University, Tianjin 300350, China

[b]Tianjin Key Laboratory of Optoelectronic Sensor and Sensing Network Technology, Nankai University, Tianjin 300350, China. E-mail: pwu@nankai.edu.cn

[c]Tianjin Key Laboratory of Micro-scale Optical Information Science and Technology, Nankai University, Tianjin 300350, China. E-mail: drliuhl@nankai.edu.cn

[d]Helmholz-Zentrum Dresden-Rossendorf, Institute of Ion Beam Physics and Materials Research, Dresden 01328, Germany.

[e]Advanced Materials Institute, Qilu University of Technology (Shandong Academy of Sciences), Jinan 250014, China.

[f]Shandong Provincial Engineering and Technical Center of Light Manipulations & Shandong Provincial Key Laboratory of Optics and Photonic Device, School of Physics and Electronics, Shandong Normal University, Jinan 250358, China.

KEYWORDS: Phase transition, swift heavy ion irradiation, relaxor ferroeletrics.

ABSTRACT

We report a novel approach of using swift O^{5+} ion irradiation to implement para-ferroelectric phase transition in a relaxor ferroelectric $KTa_{0.62}Nb_{0.38}O_3$ (KTN) single crystal. With 15-MeV swift O^{5+} ion irradiation, a well-defined two-layer structure has been formed in the KTN sample due to the interaction between the O ions and KTN via electronic stopping and the nuclear stopping, respectively. The microstructures in these two layers are characterized by using a micro-Raman (μ-Raman) spectral technique. The significant changes of both spectral intensities and locations in three characteristic Raman peaks suggest that the top layer of the KTN sample due to electronic stopping exists a single-domain-ferroelectric state with a uniform and enhanced polarization orientation along $[001]_c$ direction. More importantly, we observe the irradiated region can effectively confine the light propagation in the ferroelectric layer, which can be further controlled by external fields. The results are promising for designing new integrated photonic devices.

1. Introduction

Potassium tantalate niobate ($KTa_{1-x}Nb_xO_3$, KTN) has been receiving considerable attention as a promising functional material since 1950s, due to its large electro-optic (EO) effect, (1, 2) unique dielectric and ferroelectric properties. (3-5) With increasing temperature, the KTN crystal presents four different crystallographic structures: rhombohedral, orthorhombic, tetragonal, and cubic. (4) The transition temperature is controllable with changing the value of *x*, namely the ration of Ta:Nb in the crystal.

(6) For optical functional devices, most investigations on KTN materials are focused on the tetragonal-to-cubic transition process, as it occurs near room temperature with a proper *x* value. (7-12)

Ion implantation is a well-established technique to modify the material properties by controlling the ion-matter interaction in different ways including normal ion implantation (13-15) and swift heavy-ion irradiation. (16-18) Compared with the normal ion implantation, the swift heavy-ion irradiation exploits medium-mass ions (atomic number larger than 5, e.g., carbon, nitrogen, oxygen and fluorine, etc.) with energies above 1 MeV/amu, offering not only intriguing features with ultralow ion fluences for desired material or structure fabrications but also applicability over a wide range of materials. (19) Previous investigations have demonstrated that the ion implantation is capable of continuous modification of electric transport, magnetic properties and phase transition in metals, alloys and ferroelectric materials including $La_{0.7}Sr_{0.3}MnO_3$, $PbTiO_3$, $BiFeO_3$ and $SrRuO_3$. (20-26) Through this surface treatment with proper control of the implantation parameters, several features of the materials can be improved to a great extent.

In this work, we report a novel approach of using swift O^{5+} ion irradiation to produce the para-ferroelectric phase transition in a relaxor ferroelectric of KTN single crystal. We observe a symmetry breaking of the original lattice, revealing an off-center displacement of niobium ions and the deformation of NbO_6/TaO_6 octahedral sites due to the collisions between the irradiated O^{5+} ions and the target

atoms. We use the confocal Raman technique to study the phonon modes of the materials. The experimental results agree with the theoretical simulation based on the combination of a damped harmonic oscillator (DHO) model and the Fano function.

2. Experimental details

The KTN single crystal used in our experiment was grown by the top-seeded solution growth method. The sample was cut into dimensions of $4 \times 3 \times 2$ mm^3 with all surfaces optically polished. To produce a ferroelectric layer, one of the sample surfaces (4×3 mm^2) was irradiated with the swift oxygen (O^{5+}) ions with energy of 15 MeV and fluence of 5×10^{14} ions/cm^2 at room temperature by using the 3 MV tandem accelerator at Helmholtz-Zentrum Dresden-Rossendorf, Germany. During the irradiation, the O^{5+} ions beam was tilted by 7° off the normal direction of the sample surface to minimize the channeling effect, and the low-level ion current density (about 6-8 nA/cm^2) was kept to eliminate both heating and charging in the sample.

To characterize the microstructural change of the KTN single crystal induced by the 15 MeV swift O^{5+} ion irradiation, we measured the μ-Raman spectra of the irradiated sample by utilizing a confocal Raman spectrometer (NanoBase XperRam200) in temperatures ranging from −10 °C to 80 °C. A continuous-wave 532-nm laser beam was focused on the sample through a 40× microscope objective with numerical aperture (N.A.) of 0.75. The back-scattered Raman spectra from the sample were collected by the same objective and then propagated to a confocal slit before detected by the spectrometer. The sample temperature was increased at a 4.5

°C/min rate from −10 °C to a measuring temperature which is then kept for 3 minutes by a heating/cooling stage (Linkham THMS600) with a precision of 0.1 °C.

The morphology of the irradiated sample was characterized by using the transmission electron microscopy (TEM; FEI Tecnai G^2F20, Talos). To obtain the Curie temperature (T_c) of the KTN sample, the temperature-dependent relative dielectric constant (ε_r) measurement was performed by using an LCR meter (TH2830) with a 100 Hz, 1V sinusoidal signal.

3. Results and discussion

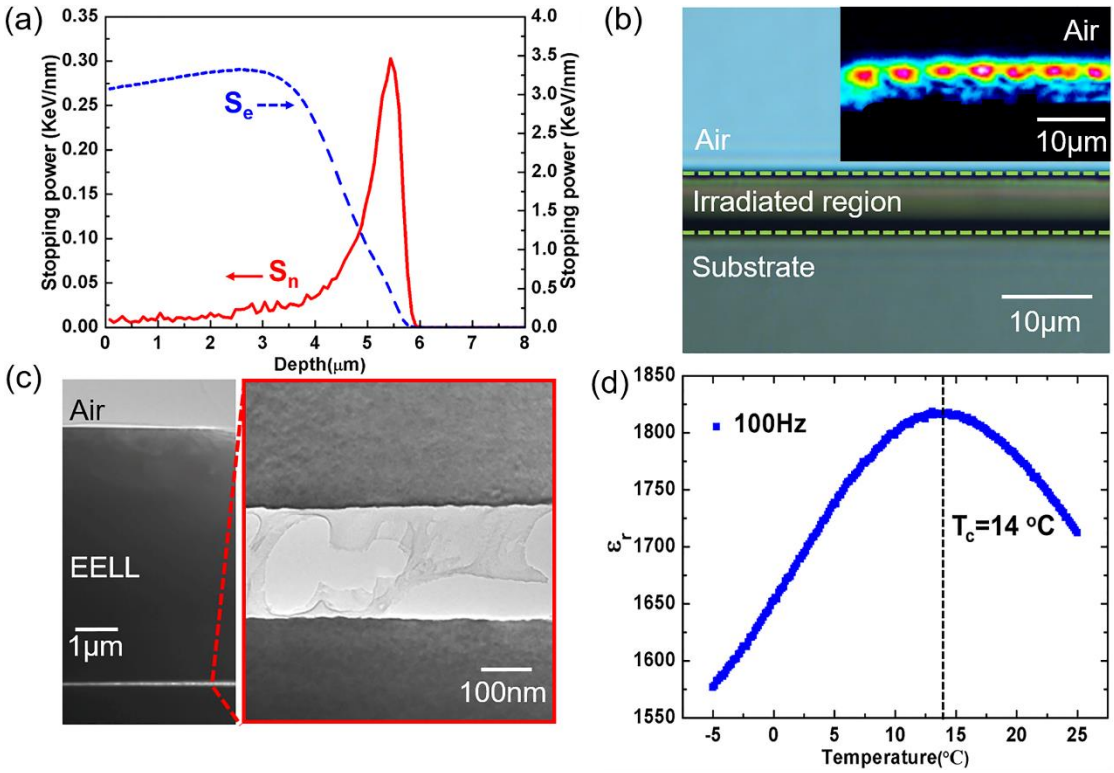

Figure 1. (a) The electronic (blue dash line) and nuclear (red solid line) stopping power profiles of the 15 MeV swift O^{5+} ion irradiated KTN crystal as a function of penetration depth from the sample surface, respectively, (b) the cross-sectional microscope image of the swift O^{5+} ion irradiated KTN crystal, and the inset shows the

near-field intensity distribution of the TE-mode for EELL at the wavelength of 632.8 nm, (c) TEM image of the cross section of the irradiated KTN crystal, (left-hand side) overall morphology and (right-hand side) partial enlarged image, (d) the relative dielectric constant versus temperature curve measured at 100 Hz for the KTN single crystal used in our experiment.

Here, a software of Stopping and Range of Ions in Matter (SRIM-2013) code was used to calculate the electronic and nuclear stopping power (S_e and S_n) profiles of 15 MeV O^{5+} ions in KTN crystal. (27) Figure 1a shows the calculated S_e and S_n results as a function of penetration depth from the sample surface irradiated with a 15 MeV swift O^{5+} ion beam. It should be noted that the S_e is dominant over the S_n from the sample surface to the depth of 4 μm. The S_e reaches its maximum of 3.25 KeV/nm around 2.7-μm depth, whereas the S_n is less than 0.03 KeV/nm. With depth exceeded 4 μm, however, the S_n increases rapidly and reaches its peak value of 0.3 KeV/nm at about 5.5-μm depth. On the other hand, the S_e decreases from its maximum and reaches zero at 6-μm depth. Based on the thermal spike model, we believe that the lattice changes occurring in the electron energy-loss layer (EELL) is primarily induced by the electronic collisions between the incident O^{5+} ions and the target atoms, leading to electronic excitation and ionization of target atoms. (28) In addition, the energy transferring from the excitation state to the lattice will result in the atomic displacement. (29)

Figure 1b shows the cross-sectional microscope image of the swift O^{5+} ion irradiated KTN crystal. It can be seen that a uniform thin layer with a depth of about 6

μm was produced at the sample surface by the O^{5+} ions irradiation. By coupling a 632.8-nm laser beam into the EELL (namely an optical well, act as a planar waveguide) via a standard end-face coupling arrangement, (30) we observed an interesting phenomenon of TE-mode optical spatial solitons (the inset of Figure 1b) occurring at room temperature. The TEM image of overall morphology on the left-hand side of Figure 1c shows an irradiated two-layer region, an electron energy-loss layer (EELL) and a nuclear energy-loss layer (NELL), which are formed by the electronic and nuclear collisions between the irradiated O^{5+} ions and the target atoms. And in the partial enlarged image displayed on the right-hand side of Figure 1c, we can see that a 200-nm thick amorphized damage (namely an optical barrier with lower refractive index) is built at about 5.5-μm depth from the surface. In consistent with Figure 1a, the location of the generated amorphous damage is just around the peak position of S_n where the value exceeds the damage threshold for the KTN sample. Both microscope image and the TEM images are in good agreement with the projected range of the 15 MeV O^{5+} ions in the KTN crystal calculated by the SRIM-2013 code, as depicted in Figures 1a. The ε_r-T curve of the KTN sample is shown in Figure 1d, indicating T_c =14 °C and the Nb-composition ratio x = 0.38 with T_c[K] = 676x + 32[K] ($x \geq 0.045$). (8)

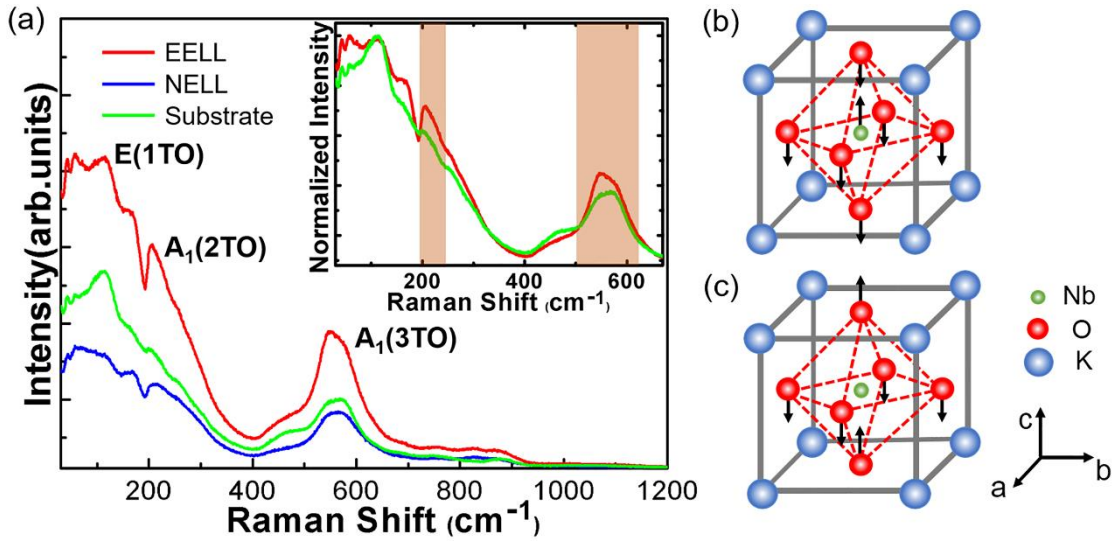

Figure 2. (a) Comparison of room temperature Raman scattering spectra obtained from the EELL at a depth of ~ 3 μm beneath the surface (red curve), the NELL (blue curve), and the substrate of the irradiated KTN sample (green curve), respectively. Inset shows the normalized Raman spectra of the EELL and substrate of the 15 MeV swift O^{5+} ion irradiated KTN crystal, schematic illustration of (b) the A_1(2TO) mode, (c) the A_1(3TO) mode, respectively.

Upon completion of the μ-Raman analysis, we found an obvious phase transition occurred in the EELL, which is observed for the first time in KTN crystal to our best knowledge. It is wellknown that the optical phonons of KTN in the cubic phase has an irreducible representation, $3T_{1u} + T_{2u}$, which are the first-order Raman inactive modes that corresponding to the space group *Pm3m* (O_h^1). However, in the tetragonal phase with *P4mm* (C_{4v}^1), each of the T_{1u} modes splits into A_1 + E modes and the T_{2u} modes splits into B_1 + E modes, satisfying the relaxing Raman selection rules as the atomic sites become lower translational symmetry during the phase transition process. As a result, all phonon modes are Raman active. (31-34) Figure 2a shows the

room-temperature Raman spectra obtained from the EELL (at the depth of 3 μm beneath the surface), the NELL, and the substrate of the irradiated KTN sample, respectively. It should be noted that the Raman spectra of EELL and substrate are normalized by the peak intensity of E(1TO) mode, as shown in the inset. In our study, we focus primarily on three characteristic Raman peaks, E(1TO), A_1(2TO), A_1(3TO), which are the key indicators showing the transformation from paraelectric phase to ferroelectric phase in KTN crystal. (35, 36) Above T_c, the presence of a Raman signature indicates that the crystalline structure of the substrate (cubic) remains in the paraelectric phase with a *Pm3m* symmetry at room temperature. In Figure 2a, it is clear that the Raman spectral intensity of the EELL is significantly enhanced with respect to the substrate. This is due to the increasing off-center displacements of niobium ions modified by electronic collisions between the incident O^{5+} ions and the target atoms, which results in a strengthening of polarization. (31, 35-37) The E(1TO) mode of the second-order Raman scattering at about 120 cm^{-1} is associated with two transverse acoustic phonons at the Brillouin zone boundary of the EELL, which is much weaker than that exited in the substrate material (see the inset) due to the effective interaction of the nucleation of the polar clusters with the transverse acoustic mode. (36-38) The A_1(2TO) mode at about 207 cm^{-1} associated with the Fano resonance corresponds to the niobium ions vibrating against all the oxygen ions of the NbO_6/TaO_6 octahedral units, as displayed in the Figure 2b. (35, 39) Compared to the substrate in cubic phase, the resonance depth of the A_1(2TO) mode is obviously enhanced in the EELL (see the inset in Figure 2b), indicating that the off-center

displacement of the Nb^{5+} ions break the lattice symmetry during the irradiation process. (6, 36) Here the peak position of A_1(2TO) for EELL is found to shift towards higher energy than that of the substrate material, which results from the expansion of the lattices induced by electronic collisions. (13, 14) In addition, the A_1(3TO) mode of the EELL at about 565 cm^{-1} ,i.e. the vibrational mode of the deformation of the NbO_6/TaO_6 octahedral units (Figure 2c), shows a noticeable anomaly in wave number as compared to the substrate. This can be attributed to the polarization enhancement of the KTN crystal in its tetragonal phase. (35, 36) As discussed above, the evolution from paraelectric cubic phase to ferroelectric tetragonal phase clearly exists in the EELL based on the experimental evidence in both the Raman peak intensity variations and the shift of peak positions. It should be noted that the microstructural changes of the EELL characterized by Raman spectra are in good agreement with the analysis by the thermal spike model mentioned in the previous section during the phase transition process from paraelectric phase to ferroelectric phase. Finally, the Raman spectral intensities in the NELL are much weaker than that in the substrate, and the peaks of A_1(2TO) and A_1(3TO) shift towards higher energies near the end of the O^{5+} ion track (shown in Figure 2a) where the lattice damage occurs due to the nuclear collisions. As a result, EELL can effectively confine the light propagation which can be further controlled by external fields.

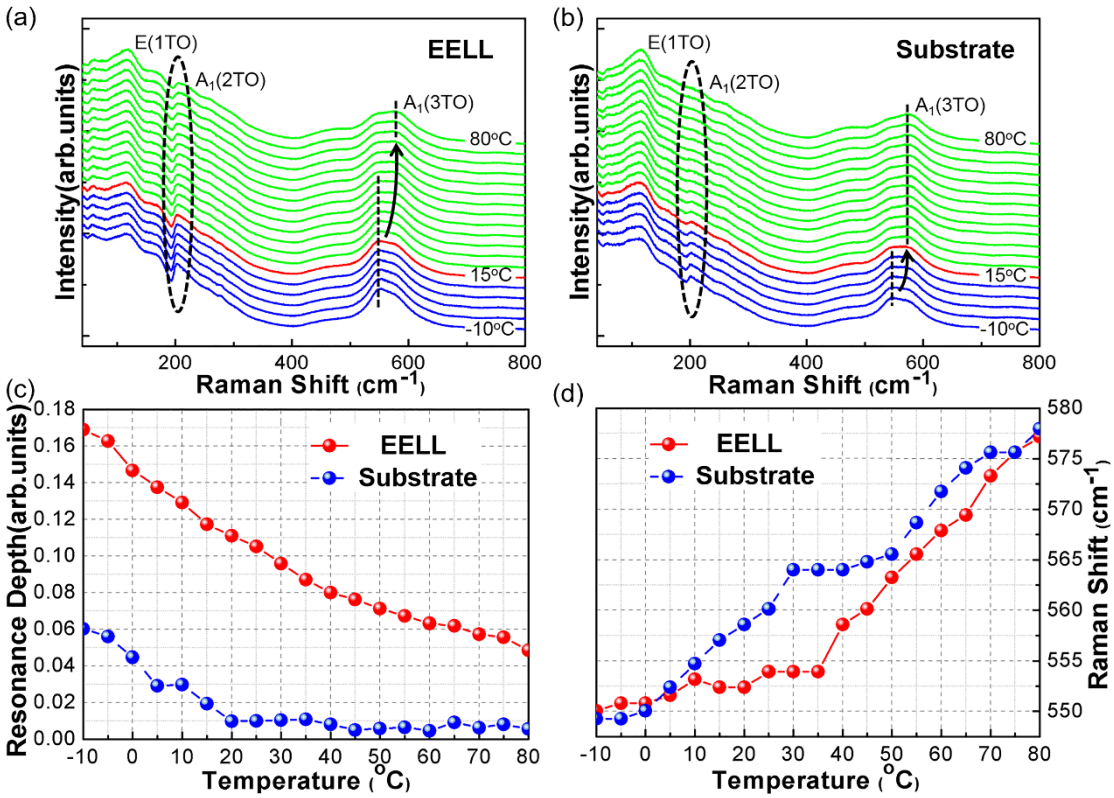

Figure 3. Raman spectra at different temperatures with an interval of 5 °C for (a) the EELL at a depth of ~ 3 μm beneath the surface and (b) the substrate of the 15 MeV swift O^{5+} ion irradiated KTN crystal. The temperature dependence of (c) the resonance depths of the A_1(2TO) mode and (d) the peak positions of the A_1(3TO) mode obtained from the EELL and the substrate of the irradiated KTN sample, respectively.

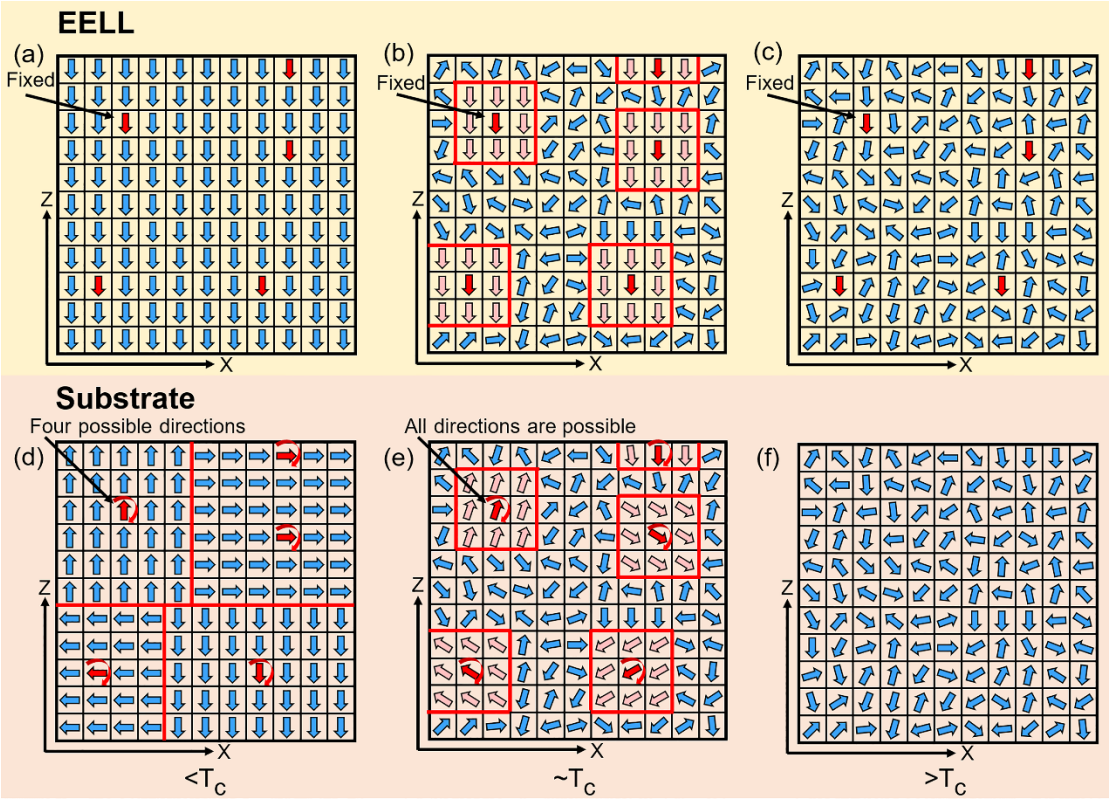

Figure 4. Diagram of polarization of (a)-(c) the EELL and (d)-(f) the substrate in the irradiated KTN sample at different phase, respectively. (a) and (d) ferroelectric phase (below T_c), (b) and (e) super paraelectric phase (in the vicinity of T_c), (c) and (f) paraelectric phase (above T_c). The ferroelectric domains of (a) the EELL oriented by the swift O^{5+} ion irradiation process and the polarization directions of the polar domains of (d) the substrate induced by the temperature in ferroelectric phase. Arrows represent the polarization directions of dipole, and red lines represent the domain walls of polar domain structures.

Figures 3a and 3b display the temperature dependent Raman spectra of the EELL (at a depth of ~ 3 μm beneath the surface) and the substrate of the KTN sample, respectively. To characterize Raman spectral changes in detail, the resonance depths of the A_1(2TO) mode and the peak positions of the A_1(3TO) mode obtained from the

EELL and the substrate of the KTN sample at different temperatures are plotted in Figures 3c and 3d. The depths of the A_1(2TO) with respect to the EELL is quite larger than that corresponding to the substrate during the entire investigation, which build up the key demonstration of the phase transition induced by the swift heavy ions in the crystal. It is clear that the ferroelectric Raman signatures at room temperature in the EELL are much noticeable compared to the spontaneous phase transition of the substrate in its ferroelectric phase when the temperature is below 15 °C. In addition, as Raman intensity is significantly enhanced in the EELL and ion irradiation can effectively control the uniaxial lattice expansion of the crystal, (14, 31) it can be demonstrated that the EELL of the KTN crystal has a single-domain-ferroelectric state with a uniform polarization orientation along $[001]_c$ direction driven by the swift O^{5+} ion irradiation, as depicted in the Figure 4a. In ferroelectric phase below T_c, the typical 90° micro-domains are formed by the spontaneous polarization process in the substrate with ordered polar domain walls in all four directions as shown in Figure 4d. (40) Along with increasing the temperature, the resonance depths of the A_1(2TO) mode gradually decreases while the wave numbers of the E(1TO) and the A_1(3TO) exhibit analogous blue shift in Figures 3a-3d, showing a clear evidence of phase transition. The results reveal that the ferroelectric domains are transformed to the polar nanoregions (PNRs) in the vicinity above the T_c (as shown in the Figures 4b and 4e). Eventually, the PNRs disappear at a certain high temperature (as shown in the Figure 4f) due to the weakening of the polarization. (35) However, upon heating to 80 °C, it is found that the resonance depth of the A_1(2TO) mode in the EELL does not

completely disappear. In other words, the PNRs remain in the cubic matrix as shown in Figure 4c, (37) revealing that the ion irradiation strengthens the polarization of polar regions due to the increasing off-center displacements of niobium ions.

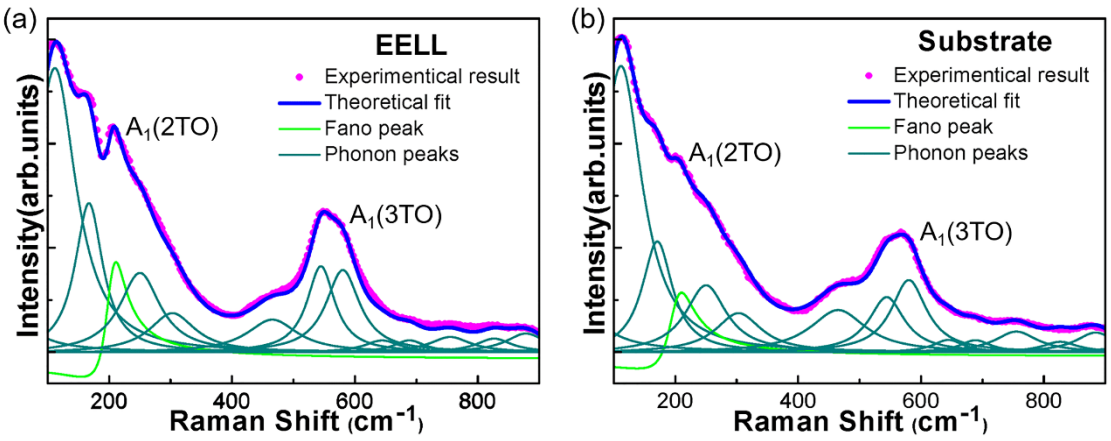

Figure 5. Fitting curves of the Raman spectra (a) the EELL and (b) the substrate of the 15 MeV swift O^{5+} ion irradiated KTN crystal at room temperature, respectively.

In the meantime, the Raman spectra of the irradiated KTN sample are fitted by the summation of a Lorentzian central peak (CP), several damped harmonic oscillators (DHO) for all phonon modes, and the Fano function with a third order polynomial (35, 41-43) as follows

$$I(\omega)=\frac{2A_{\mathrm{CP}}}{\pi}\frac{\Gamma_{\mathrm{CP}}}{4\omega^2+\Gamma_{\mathrm{CP}}^2}+\sum_i\frac{A_i\Gamma_i\omega_i^2}{\left(\omega^2-\omega_i^2\right)^2+\omega^2\Gamma_i^2}+I_{\mathrm{B}}+\frac{I_0\left(q+\varepsilon\right)^2}{\left(1+\varepsilon^2\right)}, \quad (1)$$

where A_{CP} and Γ_{CP} are intensity and full width at half maximum (FWHM) of the CP, respectively. A_{i}, Γ_{i} and ω_{i} are intensity, damping constant, and frequency of the ith Raman mode, respectively. I_{B} can be expressed as

$$I_{\mathrm{B}}=P\left(\omega-\omega_{\mathrm{TO_2}}\right)^3+Q\left(\omega-\omega_{\mathrm{TO_2}}\right)^2+R\left(\omega-\omega_{\mathrm{TO_2}}\right)^1+S, \quad (2)$$

where P, Q, R and S are constants. I_0 is intensity of the TO_2 mode (Fano

resonance), q is the asymmetry parameter, and $\varepsilon = 2(\omega-\omega_{TO2})/\Gamma_{TO2}$ where Γ_{TO2} is FWHM of the TO_2 mode, respectively. Figures 5a and 5b show the results of using Eq. (1) to fit the room-temperature Raman spectra of the EELL at a depth of ~ 3 μm (beneath the surface) and the KTN substrate, respectively. We can observe that the intensity and q of the Fano resonance of the EELL increase with respect to the substrate, while the Γ_{TO2} decreases. Our results agree well with Ref. (44). Moreover, as compared to the substrate, the intensity of DHOs associated with the A_1(3TO) mode at about 565 cm^{-1} increases and the low-wave number shoulder of the A_1(3TO) appears in the EELL, as shown in Figure 5. It should be pointed out that the presence of the Fano resonance and the anomalous change of the A_1(3TO) mode in the EELL indicate the symmetry breaking caused by the swift O^{5+} ion irradiation. (43, 44)

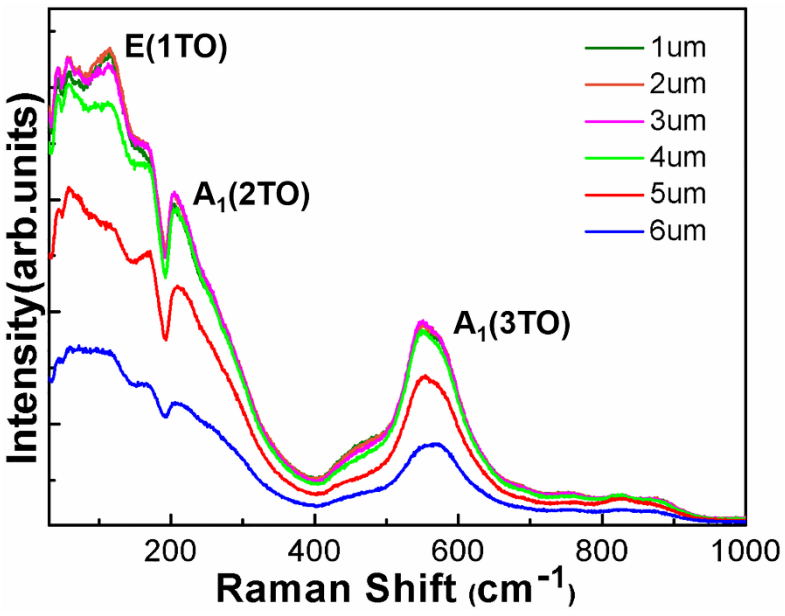

Figure 6. Comparison of room temperature Raman scattering spectra of the EELL obtained at different depths from the sample surface . The KTN crystal are irradiated by 15 MeV swift O^{5+} ions .

Furthermore, the energy of the swift heavy O^{5+} ions was transferred to the lattice gradually in the whole irradiating range, which means that the effect mentioned above should be different in the whole region. Figure 6 depicts the room-temperature Raman spectra of the EELL at different irradiated depths from the sample surface to a depth of 6 μm with an interval of 1 μm. The peak intensities and locations in the Raman spectra show no obvious changes within the first 0 - 4 μm, implying that this EELL has a relatively uniform lattice modulation. However, the Raman peak intensities gradually decrease from the depth of 4 μm to 6 μm owing to the lattice damage induced by nuclear collisions. This is in accordance with the projected range of the 15 MeV swift O^{5+} ion irradiated KTN crystal simulated by the SRIM-2013 code.

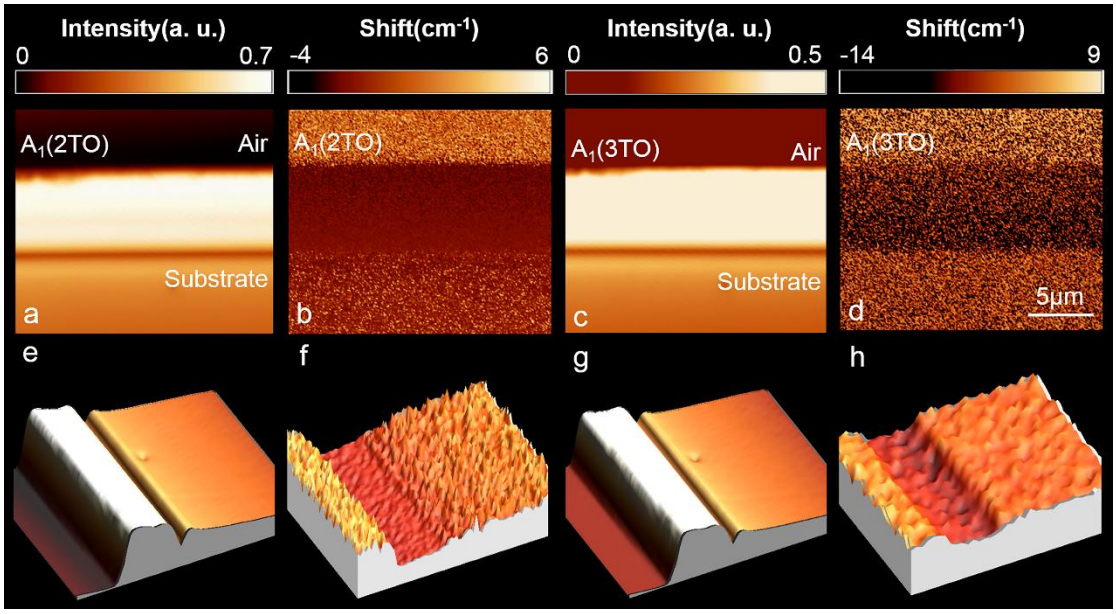

Figure 7. 2D spatial distributions of (a) intensity and (b) shift of the A_1(2TO) mode around 207 cm^{-1}, and spatial distributions of (c) intensity and (d) shift of the A_1(3TO) mode around 565 cm^{-1} obtained from the end-face of the 15 MeV swift O^{5+} ion irradiated KTN sample at room temperature, respectively, (e)-(h) correspond to the

3D spatial distributions.

Additionally, Figures 7a and 7b display the 2D spatial distributions of intensity and spectral shift of the A_1(2TO) mode, and Figures 7c and 7d correspond to the spatial distributions of intensity and the shift of the A_1(3TO) mode, respectively. Figures 7e-7h are 3D plots obtained from the end-face of the 15 MeV swift O^{5+} ion irradiated KTN sample at room temperature. It is apparent that the changes of Raman intensities and peak locations in the EELL are more pronounced with respect to the substrate. This can be attributed to the uniform and significant lattice expansion caused by the electronic collisions during the irradiation process. Near the end of the O^{5+} ion track, the strong modulation in Raman spectra contributes to the formation of a distinct gap between the EELL and the substrate.

4. Conclusion

In conclusion, we have studied the para-ferroelectric phase transition induced by swift O^{5+} ion irradiation in a relaxor ferroelectric $KTa_{0.62}Nb_{0.38}O_3$ (KTN) single crystal. Raman spectral results indicate that the EELL of the KTN sample has a single-domain-ferroelectric state with a uniformly-enhanced polarization orientation along $[001]_c$ direction induced by electronic collisions between the incident O^{5+} ions and the target atoms. The results agree well with the analysis of the microstructural changes by the thermal spike model associated with the swift O^{5+} ion irradiation process. Near the end of the O^{5+} ion track, we also observed an optical barrier capable of confining the light propagating in the optical well efficiently due to the strong optical modulation associated with the lattice damage. By combining both the

excellent ferroelectric property and the strong optical-guiding capability in a very compact size, our results are promising for integrated photonics applications such as multifunctional photonic devices and small circuit chips.

AUTHOR INFORMATION

Corresponding author：E-mail address: drliuhl@nankai.edu.cn (H. L. Liu), pwu@nankai.edu.cn (P. F. Wu). Fax: (+86)-22-23508652.

Notes

The authors declare no conflicts of interest.

ACKNOWLEDGEMENTS

This work was supported by the National Natural Science Foundation of China (NSFC) (11704201, 61575097 and 51672164); the Natural Science Foundation of Tianjin City (NSFTJ) (17JCQNJC01600); and the Natural Science Foundation of Shandong Province (Grants No. 2016ZRC01087 and ZR2017MEM016), Fundamental Research Funds for the Central Universities. Support from the Ion Beam Center of the Helmholtz-Zentrum Dresden Rossendorf (HZDR) is also acknowledged. Lei Cao acknowledges the financial support by German Research Foundation (DFG, ZH 225/10-1).

REFERENCES

[1] Hass, W.; Johannes, R. Linear electrooptic effect in potassium tantalate niobate crystals. Appl. Opt. **1967**, 6 (11), 2007–2009, DOI: 10.1364/ao.6.002007.

[2] Yu, X.; Wang, H.; Rong, X. Origin of the giant quadratic electro-optic effect in $KTa_{1-x}Nb_xO_3$ single crystals. Opt. Mater. **2015**, 46, 429-431, DOI: 10.1016/j.optmat.2015.04.059.

[3] Li, H.; Tian, H.; Gong, D. W.; Meng, Q. X.; Zhou, Z. X. High dielectric tunability of $KTa_{0.60}Nb_{0.40}O_3$ single crystal. J. App. Phys. **2013**, 114 (5), 054103, DOI: 10.1063/1.4817493.

[4] Zheng, X. J.; Zhao, H. Y.; Wang, X. P.; Liu, B.; Yu, J. D.; Zhao, X. L. Phase evolution and dielectric/ferroelectric properties of $KTa_{0.67}Nb_{0.33}O_3$ single crystal. Ceram. Int. **2015**, 41, S197-S201, DOI: 10.1016/j.ceramint.2015.03.141.

[5] Wang, X. P.; Li, Q. G.; Yang, Y. G.; Zhang, Y. Y.; Lv, X. S.; Wei, L.; Liu, B.; Xu, J. H.; Ma, L.; Wang, J. Y. Optical, dielectric and ferroelectric properties of $KTa_{0.63}Nb_{0.37}O_3$ and Cu doped $KTa_{0.63}Nb_{0.37}O_3$ single crystals. J. Mater. Sci. Mater. Electron. **2016**, 27 (12), 13075–13079, DOI: 10.1007/s10854-016-5450-0.

[6] Kallur, V. A.; Pandey, R. K. Crystal growth and properties of potassium tantalate niobate, $KTa_{1-x}Nb_xO_3$, ferroelectric. Ferroelectrics **1994**, 158 (1), 55-60, DOI: 10.1080/00150199408215993.

[7] Imai, T.; Toyoda, S.; Miyazu, J.; Kobayashi, J.; Kojima, S. Permittivity changes induced by injected electrons and field-induced phase transition in $KTa_{1-x}Nb_xO_3$ optical beam deflectors. Jpn. J. Appl Phys. **2014**, 53 (9), 09PB02, DOI: 10.7567/jjap.53.09pb02.

[8] Chang, Y.-C.; Wang, C.; Yin, S.; Hoffman, R. C.; Mott, A. G. Giant electro-optic effect in nanodisordered KTN crystals. Opt. Lett. **2013**, 38 (22), 4574–4577, DOI: 10.1364/OL.38.004574.

[9] Chen, C.-J.; Chao, J.-H.; Lee, Y. G.; Shang, A.; Liu, R.; Yin, S.; Hoffman, R. C. Enhanced electro-optic beam deflection of relaxor ferroelectric KTN crystals by

electric-field-induced high permittivity. Opt. Lett. **2019**, 44 (22), 5557-5560, DOI: 10.1364/OL.44.005557.

[10] Li, X. J.; Yang, Q. X.; Zhang, X.; He, S.; Liu, H. L.; Wu, P. F. Low DC electric-field-induced phase transition in $KTa_{0.59}Nb_{0.41}O_3$ crystal. Cryst. Growth Des. **2019**, published online, DOI: 10.1021/acs.cgd.9b01509.

[11] Zhu, W.; Chao, J. H.; Chen, C. J.; Yin, S.; Hoffman, R. C. Three order increase in scanning speed of space charge-controlled KTN deflector by eliminating electric field induced phase transition in nanodisordered KTN. Sci. Rep. **2016**, 6, 33143, DOI: 10.1038/srep33143.

[12] Inagaki, T.; Imai, T.; Miyazu, J.; Takesue, H.; Kobayashi, J. Low-voltage optical phase modulation by electric-field-induced phase transition of KTN bulk crystal. in 2014 IEEE Photonics Conference, **2014**, 390-391.

[13] Pandey, P.; Bitla, Y.; Zschornak, M.; Wang, M.; Xu, C.; Grenzer, J.; Meyer, D.; Chin, Y.; Lin, H.; Chen, C.; Gemming, S.; Helm, M.; Chu, Y.; Zhou, S. Q. Enhancing the magnetic moment of ferromagnetic $NiCo_2O_4$ via ion irradiation driven oxygen vacancies. APL Mater. **2018**, 6 (6), 066109, DOI: 10.1063/1.5036941.

[14] Chen, C.; Wang, C.; Cai, X.; Xu, C.; Li, C.; Zhou, J.; Luo, Z.; Fan, Z.; Qin, M.; Zeng, M.; Lu, X.; Gao, X.; Kentsch, U.; Yang, P.; Zhou, G.; Wang, N.; Zhu, Y.; Zhou, S.; Chen, D.; Liu, J. Controllable defect driven symmetry change and domain structure evolution in $BiFeO_3$ with enhanced tetragonality. Nanoscale **2019**, 11 (17), 8110-8118, DOI: 10.1039/c9nr00932a.

[15] Chen, F.; Tang, X.; Huang, H.; Li, X.; Wang, Y.; Huang, C.; Liu, J.; Li, H.; Chen, D. Formation of He-Rich Layers observed by neutron reflectometry in the He ions irradiated Cr/W multilayers: Effects of Cr/W interfaces on the He trapping

behavior. ACS Appl. Mater. Interfaces **2016**, 8 (37), 24300-24305, DOI: 10.1021/acsami.6b07419.

[16] Tiwari, V. K.; Avasthi, D. K.; Maiti, P. Swift Heavy Ion Induced Ordering and Piezoelectric β-phase in Poly(vinylidene fluoride). ACS Appl. Mater. Interfaces **2011**, 3 (5), 1398-1401, DOI: 10.1021/am200293g.

[17] Wylezich, H.; Mähne, H.; Rensberg, J.; Ronning, C.; Zahn, P.; Slesazeck, S.; Mikolajick, T. Local Ion Irradiation-Induced Resistive Threshold and Memory Switching in Nb_2O_5/NbO_x Films. ACS Appl. Mater. Interfaces **2014**, 6 (20), 17474-17480, DOI: 10.1021/am5021149.

[18] Pellerin, N.; Dodane-Thiriet, C.; Montouillout, V.; Beauvy, M.; Massiot, D. Cation Sublattice Disorder Induced by Swift Heavy Ions in $MgAl_2O_4$ and $ZnAl_2O_4$ Spinels: ^{27}Al Solid-State NMR Study. J. Phys. Chem. B, **2007**, 111 (44), 12707-12714, DOI: 10.1021/jp072620t.

[19] Agullo-Lopez, F.; Climent-Font, A.; Munoz-Martin, A.; Olivares, J.; Zucchiatti, A. Ion beam modification of dielectric materials in the electronic excitation regime: cumulative and exciton models. Prog. Mater. Sci. **2016**, 76, 1-58, DOI: 10.1016/j.pmatsci.2015.06.002.

[20] Uwais, Z. A.; Hussein, M. A.; Samad, M. A.; Al-Aqeeli, N. Surface Modification of Metallic Biomaterials for Better Tribological Properties: A Review. Arab. J. Sci. Eng. **2017**, 42 (11), 4493–4512, DOI: 10.1016/j.pmatsci.2015.06.002.

[21] Sharma, P.; Dhawan, A.; Sharma, S. K. Influence of nitrogen ion implantation on corrosion behavior of $Zr_{55}Cu_{30}Ni_5Al_{10}$ amorphous alloy. J. Non-Cryst. Solids **2019**, 511, 186–193, DOI: 10.1016/j.jnoncrysol.2019.02.009.

[22] Guo, H.; Dong, S.; Rack, P. D.; Budai, J. D.; Beekman, C.; Gai, Z.; Siemons, W.; Gonzalez, C. M.; Timilsina, R.; Wong, A. T.; Herklotz, A.; Snijders, P. C.; Dagotto,

E.; Ward, T. Z. Strain Doping: Reversible Single-Axis Control of a Complex Oxide Lattice via Helium Implantation. Phys. Rev. Lett. **2015**, 114 (25), 256801, DOI: 10.1103/PhysRevLett.114.256801.

[23] Saremi, S.; Xu, R. J.; Dedon, L. R.; Mundy, J. A.; Hsu, S.-L.; Chen, Z. H.; Damodaran, A. R.; Chapman, S. P.; Evans, J. T.; Martin, L. W. Enhanced electrical resistivity and properties via ion bombardment of ferroelectric thin films. Adv. Mater. **2016**, 28 (48), 10750–10756, DOI: 10.1002/adma.201603968.

[24] Saremi, S.; Xu, R. J.; Allen, F. I.; Maher, J.; Agar, J. C.; Gao, R.; Hosemann, P.; Martin, L. W. Local control of defects and switching properties in ferroelectric thin films. Phys. Rev. Mater. **2018**, 2 (8), 084414, DOI: 10.1103/PhysRevMaterials.2.084414.

[25] Herklotz, A.; Wong, A. T.; Meyer, T.; Biegalski, M. D.; Lee, H. N.; Ward, T. Z. Controlling Octahedral Rotations in a Perovskite via Strain Doping. Sci. Rep. **2016**, 6, 26491, DOI: 10.1038/srep26491.

[26] Wang, C. A.; Chen, C.; Chang, C.-H.; Tsai, H.-S.; Pandey, P.; Xu, C.; Böttger, R.; Chen, D.; Zeng, Y.-J.; Gao, X. S.; Helm, M.; Zhou, S. Q. Defect-induced exchange bias in a single $SrRuO_3$ layer. ACS Appl. Mater. Inter. **2018**, 10 (32), 27472-27476, 10.1021/acsami.8b07918.

[27] Ziegler, J. F. The Stopping and Range of Ions in Matter (SRIM-2013) code available from http://www.srim.org

[28] Wang, Z. G.; Dufour, C.; Paumier, E.; Toulemonde, M. The Se sensitivity of metals under swift-heavy-ion irradiation: a transient thermal process. J. Phys.: Condens. Matter **1994**, 6, 6733, DOI: 10.1088/0953-8984/6/34/006.

[29] Agarwal, G.; Kulshrestha, V.; Jain, R.; Kabiraj, D.; Sulania, I.; Kulriya, P.; Jain, I.P. Swift heavy ion induced effects at Mo/Si interface and silicide formation. Surf. Interf. Anal. **2009**, 41 (9), 746-752, DOI: 10.1002/sia.3083.

[30] He, R. Y.; An, Q.; Jia Y. C.; Castillo-Vega, G. R.; Vázquez de Aldana, J. R.; Chen, F. Femtosecond laser micromachining of lithium niobite depressed cladding waveguides. Opt. Mater. Express **2013**, 3 (9), 1378-1384, DOI: 10.1364/OME.3.001378.

[31] Manlief, S. K.; Fan, H. Y. Raman spectrum of $KTa_{0.64}Nb_{0.36}O_3$. Phys. Rev. B **1972**, 5 (10), 4046-4060, DOI: 10.1103/PhysRevB.5.4046.

[32] Xia, H. R.; Li, L. X.; Wang, J. Y.; Liu, Y. G.; Wei, J. Q. Soft-mode spectroscopy in Fe: $KTa_{1-x}Nb_xO_3$ crystals. Cryst. Res. Technol. **2000**, 35 (10), 1209-1214, DOI: 10.1002/1521-4079(200010)35:10<1209::AID-CRAT1209>3.0.CO;2-J.

[33] Kojima, S.; Rahaman, M. M.; Sase, R.; Hoshina, T.; Tsurumi, T. Vibrational dynamics of ferroelectric $K(Ta_{1-x}Nb_x)O_3$ studied by far-infrared spectroscopic ellipsometry and Raman scattering. Jpn. J. Appl. Phys. **2018**, 57, 11UB05, DOI: 10.7567/JJAP.57.11UB05.

[34] Hawley, C. J.; Wu, L.; Xiao, G.; Grinberg, I.; Rappe, A. M.; Davies, P. K.; Spanier, J. E. Structural and ferroelectric phase evolution in $[KNbO_3]_{1-x}[BaNi_{1/2}Nb_{1/2}O_{3-\delta}]_x$ (x = 0, 0.1). Phys. Rev. B **2017**, 96, 054117, DOI: 10.1103/physrevb.96.054117.

[35] Wang, Y.; Meng, X. D.; Tian, H.; Hu, C. P.; Xu, P.; Tan, P.; Zhou, Z. X. Dynamic evolution of polar regions in $KTa_{0.56}Nb_{0.44}O_3$ near the para-ferroelectric phase transition. Cryst. Growth Des. **2019**, 19 (2), 1041–1047, DOI: 10.1021/acs.cgd.8b01576.

[36] Bartasyte, A.; Kreisel, J.; Peng, W.; Guilloux-Viry, M. Temperature-dependent Raman scattering of $KTa_{1-x}Nb_xO_3$ thin films. Appl. Phys. Lett. **2010**, 96 (26), 262903, DOI: 10.1063/1.3455326.

[37] Chen, C. J.; Zhu, W.; Chao, J. H.; Shang, A.; Lee, Y. G.; Liu, R.; Yin, S.; Dubinskii, M.; Hoffman, R. C. Study of thermal and spatial dependent electric field-induced phase transition in relaxor ferroelectric crystals using Raman spectroscopy. J. Alloys Compd. **2019**, 804, 35-41, DOI: 10.1016/j.jallcom.2019.06.200.

[38] Svitelskiy, O.; Toulouse, J. Translational and rotational mode coupling in disordered ferroelectric $KTa_{1-x}Nb_xO_3$ studied by Raman spectroscopy. J. Phys. Chem. Solids **2003**, 64 (4), 665-676, DOI: 10.1016/S0022-3697(02)00369-4.

[39] Wang, D.; Hlinka, J.; Bokov, A. A.; Ye, Z. G.; Ondrejkovic, P.; Petzelt, J.; Bellaiche, L. Fano resonance and dipolar relaxation in lead-free relaxors. Nat. Commun. **2014**, 5, 5100, DOI: 10.1038/ncomms6100.

[40] Zhang, X.; Yang, Q. X.; Liu, H. L.; Wang, X. P.; He, S.; Wu, P. F. Switching effects of spontaneously formed superlattices in relaxor ferroelectrics. Opt. Mater. Express **2019**, 9 (10), 4081-4089, DOI: 10.1364/OME.9.004081.

[41] Toulouse, J.; Jiang, F.; Svitelskiy, O.; Chen, W.; Ye, Z. G. Temperature evolution of the relaxor dynamics in $Pb(Zn_{1/3}Nb_{2/3})O_3$: A critical Raman analysis. Phys. Rev. B **2005**, 72 (18), 184106, DOI: 10.1103/PhysRevB.72.184106.

[42] Yacoby, Y. Defect induced fluctuations in the paraelectric phase of $KTa_{0.94}Nb_{0.06}O_3$. Z. Physik B **1978**, 31, 275-282, DOI: 10.1007/bf01352352.

[43] Rahaman, M. M.; Imai, T.; Sakamoto, T.; Helal, M. A.; Tsukada, S.; Kojima, S. Ferroelectric phase transition of Li-doped $KTa_{1-x}Nb_xO_3$ single crystals with weak

random fields: Inelastic light scattering study. J. Alloy Compd. **2018**, 735, 1063-1070, DOI: 10.1016/j.jallcom.2017.11.039.

[44] Slodczyk, A.; Daniel, P.; Kania, A. Local phenomena of (1-x)$PbMg_{1/3}Nb_{2/3}O_3$-x$PbTiO_3$ single crystals ($0 \leq x \leq 0.38$) studied by Raman scattering. Phys. Rev. B **2008**, 77 (18), 184114, DOI: 10.1103/PhysRevB.77.184114.